Broadband and Energy-Concentrated Absorber Based on Hemispherical-Embedded Structure

Zhe Wu, Zhongzhu Liang,* Xiaoyan Shi, Fuming Yang, Rui Dai, Enzhu Hou, Wenwen Sun, Zheng Qin, Wei Xin, and Haiyang Xu

Spatially concentrated absorption is able to form local hotspots and helps to generate hot electrons with higher energy than free electrons, which can be used to improve the performance of hot electron devices. Herein, a broadband, wide-angle, and highly concentrated metamaterial absorber operating in near-infrared and midinfrared bands is proposed. The absorptivity of the proposed absorber exceeds 90% in the wavelength range of 2.0–5.4 μm, and the average absorptivity at 2.0–5.4 μm reaches 93.5%. Moreover, the absorber can highly concentrate the energy of the incident light on a point on the bottom surface of the device; the area with concentrated energy only accounts for 1.4% of the total area of the bottom, thus forming a hotspot. Meanwhile, the absorber can still maintain an average absorptivity of more than 85% when the incident light angle of various polarization directions reaches 60°. These characteristics enable the device to provide a solution to improve the performance of hot electrons, energy collection, and imaging devices.

Z. Wu, Z. Liang, X. Shi, F. Yang, R. Dai, E. Hou, W. Sun, W. Xin, H. Xu
Center for Advanced Optoelectronic Functional Materials Research and
Key Laboratory of UV Light-Emitting Materials and Technology of Ministry
of Education
College of Physics
Northeast Normal University
Changchun 130024, China
E-mail: liangzz@nenu.edu.cn

Z. Liang, X. Shi, F. Yang, Z. Qin
State Key Laboratory of Applied Optics
Changchun Institute of Optics, Fine Mechanics and Physics, Chinese
Academy of Sciences
Changchun, Jilin 130033, China

Z. Liang, X. Shi, Z. Qin
University of the Chinese Academy of Sciences
China

Z. Qin
Interdisciplinary Center for Fundamental and Frontier Sciences
Nanjing University of Science and Technology
Jiangyin, Jiangsu 214443, China

1. Introduction

Recently, metamaterial devices have attracted substantial attention due to their marvelous electromagnetic performance in many applications such as antenna systems,[1] electromagnetic cloaking,[2,3] imaging,[4] ultrasensitive sensing,[5,6] and refractive index engineering.[7,8] In these domains, broadband strong absorption is critical for performance. In the last decades, extensive research has focused on achieving multiband or broadband absorption.[2,3,9–12] In the infrared band, the general strategy to increase the absorption bandwidth is to use a supercell configuration that integrates multiple coplanar resonators,[6,11,12] such as multiple sizes of crosses, disks, and ellipses, to obtain multiple localized surface plasmon resonances (LSPRs). Another strategy is combining the LSPR and propagating surface plasmon resonances (PSPRs) to realize broadband strong absorption.[13–16] Another strategy is to use nanostructured metals or even highly doped silicon that can behave as black metasurfaces over ultrabroadband.[17] High-performance broadband metamaterial absorbers (MAs) are widely used in many practical applications, especially in improving the performance of hot electron devices.

There are currently extensive interests on the hot electron-mediated photoconversion. However, the device quantum yield is fundamentally low due to the existence of various hot electron loss channels. The previous strategy was to distinguish the thermodynamic losses in hot electron devices to improve the performance.[18] Plasmonic energy conversion has been proposed as a promising alternative to conventional electron–hole separation in semiconductor devices,[19–23] which plays a vital role in practical applications in multiple fields, such as photodetectors,[23–27] photovoltaics,[28–35] sensing,[36] photocatalysis,[37–41] and microbolometers.[42,43] Spatially, concentrated absorption is conducive to creating local hotspots to generate hot electrons with higher energy than free electrons, which can be used in hot electron devices to improve their performance.

In this article, we proposed a broadband, wide-angle, and highly concentrated MA operating in near-infrared and midinfrared bands. Firstly, we proposed a structure consisting of a metal hemisphere embedded in insulator layer and a surface pattern placed directly above the center of the hemisphere. The proposed absorber exhibits broadband absorption of near-infrared

**ADVANCED
SCIENCE NEWS**

www.advancedsciencenews.com

**ADVANCED
PHOTONICS
RESEARCH**

www.adpr-journal.com

and midinfrared wavelength due to the excitation of surface plasmon polariton (SPP), LSPR, and gap plasmon resonance (GPR). Next, we verified the contribution of the SPP mode, indicating that it is able to couple the light into the air slot, which enhances the GPR, further enhancing the absorption rate and absorption bandwidth. Subsequently, we characterized the energy density of the device in the x–z plane and x–y plane and found that it can highly concentrate the energy of incident light on a point at the bottom surface of the absorber. Specifically, the area with concentrated energy only accounts for 1.4% of the total area of the bottom, and the energy ratio between the bottom tangent point and the bottom spherical center point (ERTC) is 3.2×10^{11}; the energy of structure tangent point with surface pattern is 21.5% higher than that without surface pattern, and the ERTC is 5.8 times that without a surface pattern, thus forming a hotspot, whose position is related to the polarization angle of the incident light. Finally, we characterized the polarization and incident angle tolerance of the proposed absorber and proved that the proposed device holds excellent characteristics of polarization and incident angle insensitivity. These excellent characteristics suggest that the proposed absorber has promising application in high-performance plasmonic hot electron devices.

2. Modeling and Simulation

Figure 1a shows the proposed broadband MA with a magnified unit cell. The proposed broadband metamaterial from bottom to top consists of a titanium (Ti) hemisphere embedded in Al_2O_3 insulator and a Ti cube placed on the surface as a pattern directly above the center of the hemisphere. The Al_2O_3 insulator is tangent to the hemisphere, which means its length and width are equal to the diameter of the hemisphere and its thickness is equal to the radius of the hemisphere. The specific geometric parameters to characterize the proposed MA are as follows: the diameter of the hemisphere $d = 2\,\mu m$, the length and width of surface cube pattern $l = w = 0.8\,\mu m$, and the thickness of surface pattern $t = 0.6\,\mu m$, respectively. Since the hemisphere is tangent to the edge of unit cell, naturally, it is also tangent to the adjacent hemispheres, which forms a compact hemispherical

array embedded in the insulator structure with surface patterns directly above it. To verify the absorber's performance, we performed a simulation using the finite-difference time domain method; other numerical algorithm methods are used for verification, and the results are consistent.[44–46] The material parameters of Ti and Al_2O_3 were obtained from Rakić[47] and Querry,[48] respectively. The light is vertically incident along the negative direction of the z-axis, and the electric field propagates along the x-axis. Periodic boundary conditions are used in x- and y-directions, and perfectly matched layer (PML) boundary is used in z-direction.

3. Optical Properties and Physical Mechanisms

The performance of the proposed MA is shown in Figure 1b. The absorption spectrum of the absorber is calculated from the reflectance and transmittance, obtained by simulation, using $A = 1$-R-T, where R and T are reflectivity and transmissivity, respectively. It can be seen from the spectrum that there are three absorption peaks in the simulated wavelength band (Figure 1b red line), respectively, located at 2.0, 2.6, and 4.5 μm, marked as P1, P2, and P3. The absorption rate at P1, P2, and P3 reached 93.0%, 94.2%, and 95.7%, respectively. Meanwhile, the absorber shows rather broadband absorption higher than 90% covering the range from 2.0 to 5.4 μm, and the average absorptivity at 2–5.4 μm reaches 93.5%.

To further reveal the physical mechanism of the broadband absorption, we calculated the distribution of the electromagnetic field at the wavelengths of the absorption peaks in the x–z plane. As shown in **Figure 2**a–c, it is clearly observed from the electric field distributions that SPPs are excited in the metamaterial structure where light is coupled into the air slot and localized around the metal corners between the adjacent unit cells, creating the SPP-induced light absorption. Nevertheless, the distributions of the magnetic field are totally different. In specific, at the short wavelength of P1 shown in Figure 2d, the magnetic field is concentrated at the upper surface of the surface patterns as well as the tangent point and its adjacent spaces between hemispheres, indicating that LSPR and GPR are excited. As shown in
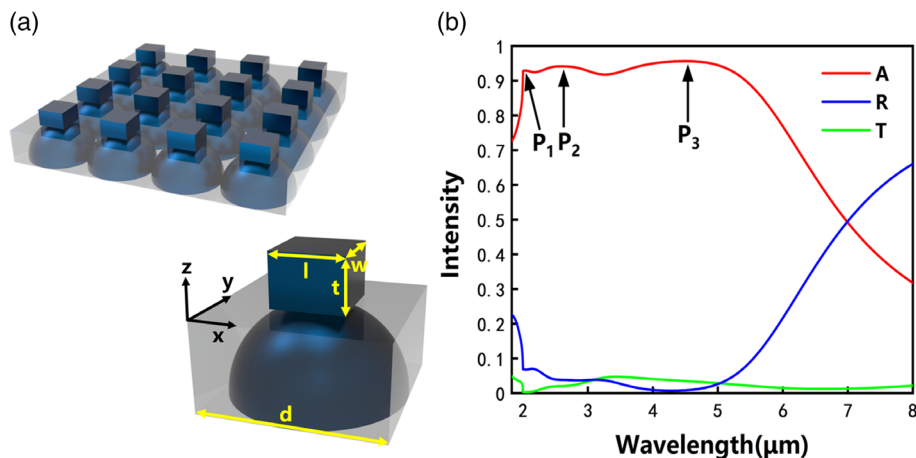

Figure 1. a) Schematic diagram of the proposed broadband MA. With the geometric parameters: $d = 2\,\mu m$, $l = w = 0.8\,\mu m$, $t = 0.6\,\mu m$. b) Absorption, reflective, and transmission spectrum of the proposed absorber.
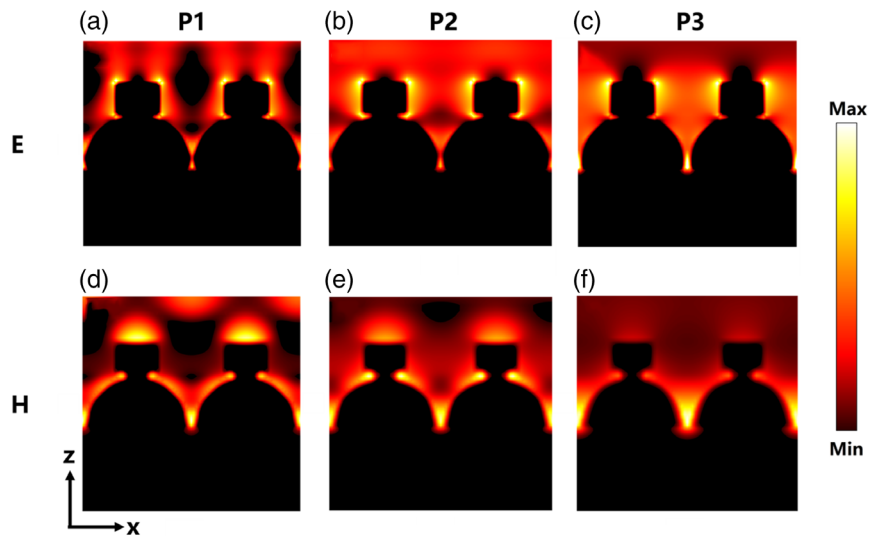
Figure 2. Electric field distribution of the proposed absorber at the a) absorption peak 1, b) 2, and c) 3 in x–z plane. Magnetic distribution of the proposed absorber and the absorption peak d) 1, e) 2, and f) 3 in x–z plane.

Figure 2e, the magnetic field at P2 is concentrated at the tangent points and their adjacent spaces between hemispheres and between hemispheres and surface patterns. Furthermore, it is obvious in Figure 2c,f that the electric and magnetic field at P3 are highly concentrated at the tangent points and their adjacent spaces between hemispheres. Therefore, the broadband absorption of our proposed MA is caused by hybrid mode of SPP, LSPR, and GPR.

As optical impendence matching plays an important role in areas of MAs, we retrieve the corresponding effective optical impendence to get further insight into the proposed structure. We calculated the equivalent impendence of the absorber by[49]

$$Z = \sqrt{\frac{(1 + S_{11})^2 - S_{21}^2}{(1 - S_{11})^2 - S_{21}^2}} \qquad (1)$$

Here $Z = Z' + iZ''$. The equivalent impendence is calculated from the scattering parameters S_{11} and S_{21}, which denote the scattering matrix coefficients of normal incidence reflection and transmission in transverse magnetic (TM) polarization, respectively. The impendence of air is considered to be $Z_{air} = 1$. The real and imaginary parts of the equivalent impendence both contribute to the absorptivity of the absorber; according to $R = \frac{(Z'-1)^2 + (Z'')^2}{(Z'+1)^2 + (Z'')^2}$,[49] perfect absorption occurs at the wavelength where the equivalent impendence is perfectly matched to air. **Figure 3**b shows the simulation results for the normalized real and imaginary parts of the optical impendence for the proposed absorber. It can be clearly seen that both the real and imaginary parts are matched to the Z_{air} values of 1 and 0 in the wide absorption wavelength range, resulting in highly efficient broadband absorption.

4. Influence of Surface Patterns on the Performance of MAs

To additionally verify the contribution of SPP mode to broadband absorption, we compare the absorption spectrum of the proposed
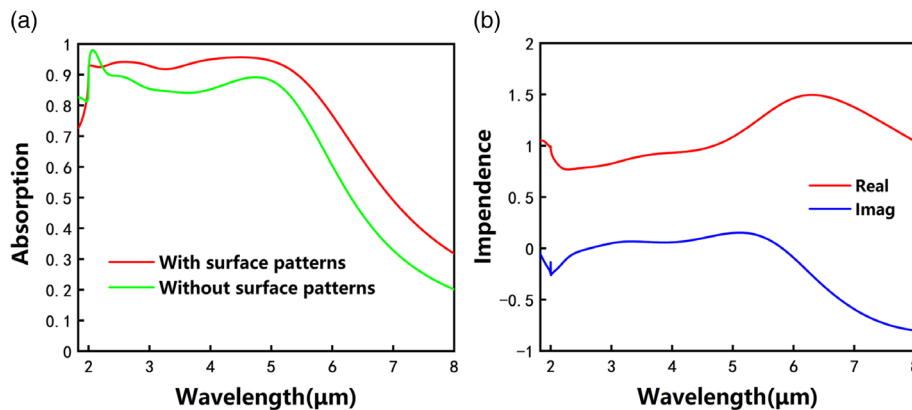

Figure 3. a) Absorption spectrum of the proposed absorber with surface pattern (red line) and without surface pattern (green line). b) The real part (red line) and imaginary part (blue line) of equivalent impendence of the proposed absorber.

2200301 (3 of 7)

structure without the surface patterns, where the hemispheres and insulators are identical to those of the proposed one. The spectra of both cases are shown in Figure 3a. It is not hard to see that the structure without surface patterns has a stronger absorption peak with an absorption rate of 98.0% at the wavelength of 2.1 μm (green line), which is caused by the GPR between the hemispheres. The reason why the absorptivity of the proposed structure with surface patterns at this wavelength is lower than that of the structure without surface patterns is that the surface patterns blocks part of the light from reaching the surface of the hemisphere to achieve energy concentration, and LSPR and GPR have certain competition in light absorption. In addition, the absorption of the proposed structure with surface patterns at the rest of the wavelength band is higher than that without surface patterns. Specifically, the average absorptivity of the structure without surface patterns at 2–5.5 μm is only 88%, which is 5.5% lower than the proposed structure. The reason for this part of enhancement is that SPP mode couples light into the air slot directly above the hemisphere tangent points, thus enhancing the GPR-dominated absorption mode and widening the absorption bandwidth and enhancing the absorption rate.

5. Analysis of Energy Concentration

Furthermore, we plotted the energy density of the proposed structure in the x–y and x–z planes at the three absorption peaks under the TM wave incidence condition (electric field is along the x-direction), as shown in **Figure 4**. The different colors in the figure represent the gradient of normalized energy intensity after taking the logarithm. From Figures 4a–c, we can see that the thermal is concentrated at the tangent point and its adjacent space between the hemispheres. Meanwhile, from Figures 4d–f, it can be seen that the thermal is highly concentrated at the tangent point located at the bottom surface of the proposed device. **Figure 5**a,b shows the normalized intensity of energy density on the x-axis (at y = 1 μm) and y-axis (at x = 0 μm) on the bottom surface of the proposed device at peak 3; it can be seen that there are strong peaks of energy at the tangent point. Specifically, the area with concentrated energy only accounts for 1.4% of the total area of the bottom, and the energy ratio between the bottom tangent point and the bottom spherical center point (ERTC) is 3.2×10^{11}; the energy of structure tangent point with surface pattern is 21.5% higher than that without surface pattern, and the ERTC is 5.8 times that without surface pattern. In the absorption process, the metal has ohmic loss, while the insulator is photon–phonon conversion, both of which result in heat generation. So the energy of light is converted to thermal energy and highly concentrated at the bottom surface to generate local hotspots to generate hot electrons with higher energy than free electrons, which can be used in hot electronic devices to improve their performance.

6. Polarization Sensitivity of Energy-Concentrated Point

In addition, the proposed structure also shows that the position of the thermal concentration point is sensitive to the polarization angle. We simulated the energy density on the bottom surface of the proposed structure at P3 under the polarization angles of 0° (TM), 45°, and 90° (transverse electric (TE)), as shown in **Figure 6**. Compared Figure 6a,c, the thermal concentration points are significant at different positions. When the electric field propagates along the x-direction (under TM mode), the thermal concentration point is at the tangent points along the x-axis. Correspondingly, when the electric field propagates along the y-direction (under TE mode), the thermal concentration point is at the tangent points along the y-axis. However, when the polarization angle is 45°, it can be clearly seen from Figure 6b that the thermal is concentrated at tangent points along both x-axis and y-axis. When the proposed device is used in combination with
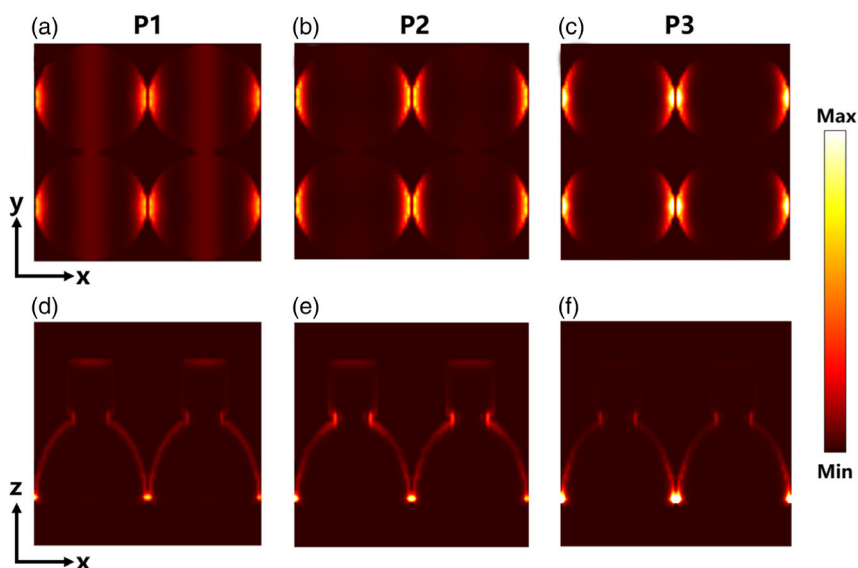

Figure 4. Energy density at the bottom surface of the absorber at the a) absorption peak 1, b) 2, and c) 3 in x–y plane. Energy density in x–z plane at the d) absorption peak 1, e) 2, and f) 3.

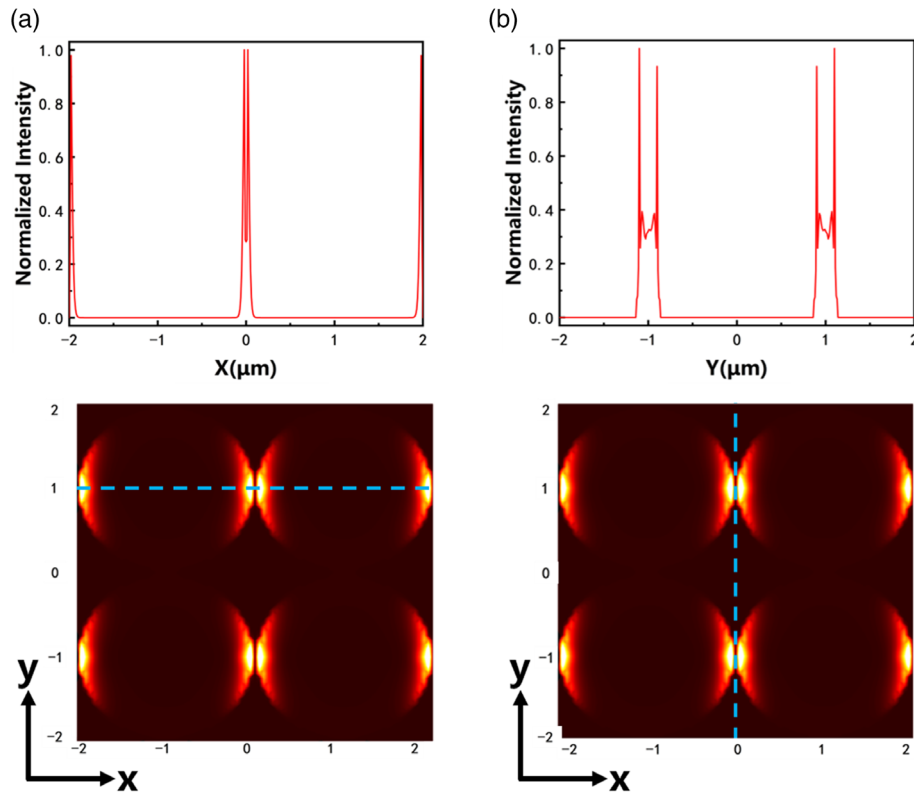**Figure 5.** a) Normalized intensity of energy density on the *x*-axis (at *y* = 1 μm) on the bottom surface of the proposed device at peak 3 under TM mode (the electric field propagates along the *x*-direction). b) Normalized intensity of energy density on the *y*-axis (at *x* = 0 μm) on the bottom surface of the proposed device at peak 3 under TM mode (the electric field propagates along the *x*-direction).
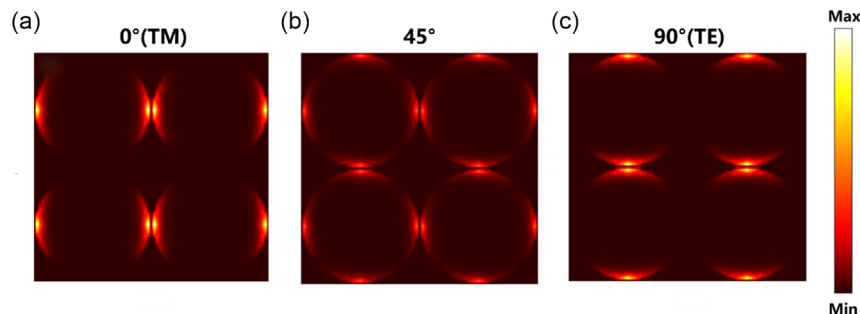

Figure 6. Energy density at the bottom surface of the proposed absorber at peak 3 under the polarization angles of 0° a), 45° b), and 90° c).

thermistors below the tangent points, a unique time harmonic current will be generated when a beam of dynamically changing polarization light is incident on the device. Therefore, this device can be used for dynamic polarization state detection, information encryption, and other practical applications.

7. Wide-Angle Absorption

For practical applications such as thermal harvesting, cloaks, and microbolometers, existing infrared devices often work under a larger incident angle, so the ability to maintain high absorption

for unpolarized light within a wide incident angle range for the absorber is usually required. To verify the polarization and incident angle characteristics of the absorber, we calculated the absorption spectrum with a polarization angle of 0°–90° by scanning at each step of 10°, as shown in **Figure 7**a. When the polarization angle of the incident light changes from 0° to 90°, the absorption spectrum did not change and shows the characteristic of polarization insensitivity, which benefits from the symmetry of our unit cell structure. Moreover, to characterize the dependence of the absorber's performance on the incident angle, we performed scanning simulation with an incident angle of 0°–60° and a step angle of 10° under TM, TE, and unpolarized
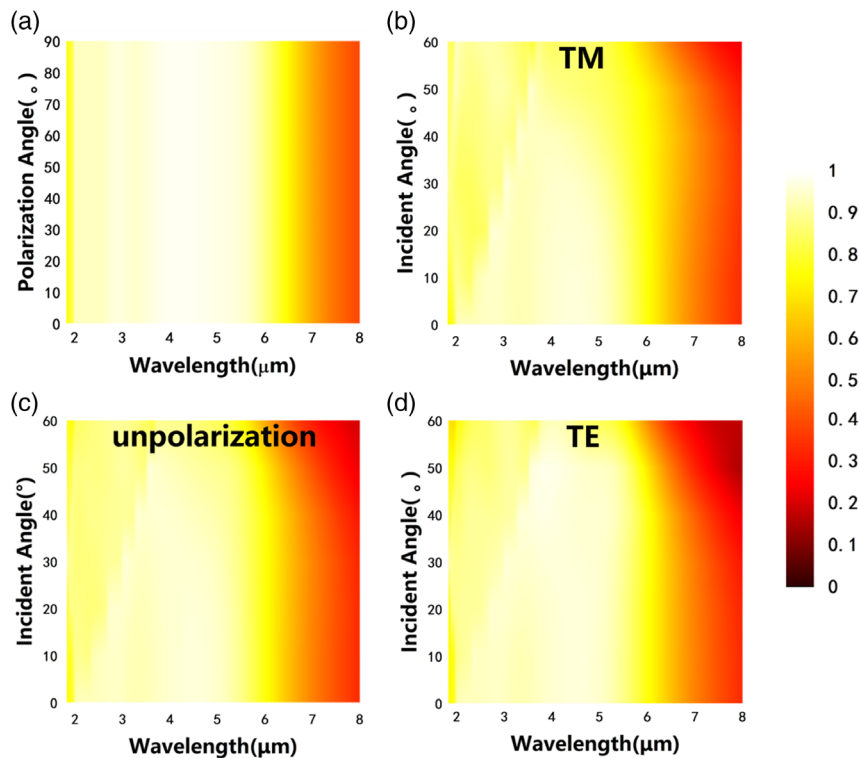
Figure 7. The dependence of the absorber's performance on the a) polarization angle, b) TM-wave incident angle, c) unpolarized-wave incident angle, and d) TE-wave incident angle.

light, as shown in Figures 7b–d. We can see in Figures 7b–d that whether for TM, TE, or unpolarized light, with the increase of incident angle, the absorptivity of the proposed absorber only shows a slight decrease at the short-wavelength band, and the average absorptivity under TM, TE, and unpolarized light still remains above 88%, 85%, and 86%, respectively. It indicates that the proposed absorber holds excellent characteristics of polarization and incident angle insensitivity.

8. Conclusion

In summary, we proposed a broadband, polarization, and incident angle-insensitive MA with energy highly concentrated at the bottom surface and the absorption band covering two atmospheric transparency windows. First, we proposed a structure consisting of a metal hemisphere embedded in the insulator layer and a surface pattern placed directly above the center of the hemisphere. The proposed absorber exhibits broadband absorption of near-infrared and midinfrared wavelength due to the excitation of SPP, LSPR, and GPR. Moreover, we verified the contribution of the SPP mode, which is able to enhance the absorption rate and absorption bandwidth. Subsequently, we characterized the energy density of the device in the x–z plane and x–y plane and found that it can highly concentrate the energy of incident light on a point at the bottom surface of the absorber; the area with concentrated energy only accounts for 1.4% of the total area of the bottom, and its position is related to the polarization angle of the incident light, and the energy ratio between

the bottom tangent point and the bottom spherical center point (ERTC) is 3.2×10^{11}; the energy of structure tangent point with surface pattern is 21.5% higher than that without surface pattern, and the ERTC is 5.8 times that without surface pattern. Finally, we characterized the polarization and incident angle tolerance of the proposed absorber and proved that the absorber can still maintain an average absorptivity of more than 85% when the incident light angle of various polarization directions reaches 60°. These excellent characteristics suggest that the proposed absorber has promising application in high-performance plasmonic hot electron devices.

Conflict of Interest

The authors declare no conflict of interest.

Data Availability Statement

The data that support the findings of this study are available from the corresponding author upon reasonable request.

[1] H. O. Yilmaz, F. Yaman, *IEEE Trans. Instrum. Meas.* **2020**, *69*, 1775.
[2] D. Shin, Y. Urzhumov, Y. Jung, G. Kang, S. Baek, M. Choi, H. Park, K. Kim, D. R. Smith, *Nat. Commun.* **2012**, *3*, 1213.
[3] S. S. Islam, M. R. I. Faruque, M. T. Islam, *Mater. Res. Bull.* **2017**, *96*, 250.
[4] S. Jiang, J. Li, J. Li, J. Lai, F. Yi, *Opt. Express* **2022**, *30*, 9065.
[5] Y. Li, X. Wang, Y. Liu, W. Jin, H. Tian, F. Xie, K. Xia, X. Zhang, W. Fu, Y. Zhang, *Front. Bioeng. Biotechnol.* **2022**, *10*, 1071472.
[6] Y. Kim, H. Kim, Y. Yang, T. Badloe, N. Jeon, J. Rho, *Nanoscale* **2022**, *14*, 3720.
[7] S. H. Lee, J. Choi, H.-D. Kim, H. Choi, B. Min, *Sci. Rep.* **2013**, *3*, 2135.
[8] S. Datta, S. Mukherjee, X. Shi, M. Haq, Y. Deng, L. Udpa, E. Rothwell, *Sensors* **2021**, *21*, 4782.
[9] Y. Zhang, Z. Yi, X. Wang, P. Chu, W. Yao, Z. Zhou, S. Cheng, Z. Liu, P. Wu, M. Pan, Y. Yi, *Phys. E* **2021**, *127*, 114526.
[10] B.-X. Wang, C. Xu, G. Duan, J. Jiang, W. Xu, Z. Yang, Y. Wu, *Nanoscale Res. Lett.* **2022**, *17*, 115.
[11] C. Zhang, S. Yin, C. Long, B. W. Dong, D. He, Q. Cheng, *Opt. Express* **2021**, *29*, 14078.
[12] W. Yu, Y. Lu, X. Chen, H. Xu, J. Shao, X. Chen, Y. Sun, J. Hao, N. Dai, *Adv. Opt. Mater.* **2019**, *7*, 1900841.
[13] Y. Zhou, Z. Qin, Z. Liang, D. Meng, H. Xu, D. R. Smith, Y. Liu, *Light Sci. Appl.* **2021**, *10*, 138.
[14] X. Shi, Z. Qin, Z. Liang, D. Meng, J. Li, S. Zhang, R. Dai, E. Hou, W. Xin, H. Liu, H. Xu, Y. Liu, *Opt. Express* **2022**, *30*, 20532.
[15] Z. Qin, X. Shi, F. Yang, E. Hou, D. Meng, C. Sun, R. Dai, S. Zhang, H. Liu, H. Xu, Z. Liang, *Opt. Express* **2022**, *30*, 473.
[16] Z. Qin, D. Meng, F. Yang, X. Shi, Z. Liang, H. Xu, D. R. Smith, Y. Liu, *Opt. Express* **2021**, *29*, 20275.
[17] S. Sarkar, *Adv. Photonics Res.* **2022**, *3*, 2200223.
[18] C. Zhang, G. Cao, S. Wu, W. Shao, V. Giannini, S. A. Maier, X. Li, *Nano Energy* **2019**, *55*, 164.
[19] C. Clavero, *Nat. Photonics* **2014**, *8*, 95.
[20] A. Sobhani, M. W. Knight, Y. Wang, B. Zheng, N. S. King, L. V. Brown, Z. Fang, P. Nordlander, N. J. Halas, *Nat. Commun.* **2013**, *4*, 1643.
[21] K. Wu, J. Chen, J. R. McBride, T. Lian, *Science* **2015**, *349*, 632.
[22] H. Shan, Y. Yu, X. Wang, Y. Luo, S. Zu, B. Du, T. Han, B. Li, Y. Li, J. Wu, F. Lin, K. Shi, B. K. Tay, Z. Liu, X. Zhu, Z. Fang, *Light Sci. Appl.* **2019**, *8*, 9.
[23] W. Li, J. G. Valentine, *Nanophotonics* **2017**, *6*, 177.
[24] H. Wang, P. Zhang, Z. Zang, *Appl. Phys. Lett.* **2020**, *116*, 162103.
[25] W. Li, J. Valentine, *Nano Lett.* **2014**, *14*, 3510.
[26] W. Li, Z. J. Coppens, L. V. Besteiro, W. Wang, A. O. Govorov, J. Valentine, *Nat. Commun.* **2015**, *6*, 8379.

[27] X. Cai, A. B. Sushkov, R. J. Suess, M. M. Jadidi, G. S. Jenkins, L. O. Nyakiti, R. L. Myers-Ward, S. Li, J. Yan, D. K. Gaskill, T. E. Murphy, H. D. Drew, M. S. Fuhrer, *Nat. Nanotechnol.* **2014**, *9*, 814.
[28] C. Yan, J. Huang, K. Sun, S. Johnston, Y. Zhang, H. Sun, A. Pu, M. He, F. Liu, K. Eder, L. Yang, J. M. Cairney, N. J. Ekins-Daukes, Z. Hameiri, J. A. Stride, S. Chen, M. A. Green, X. Hao, *Nat. Energy* **2018**, *3*, 764.
[29] J. E. Spanier, V. M. Fridkin, A. M. Rappe, A. R. Akbashev, A. Polemi, Y. Qi, Z. Gu, S. M. Young, C. J. Hawley, D. Imbrenda, G. Xiao, A. L. Bennett-Jackson, C. L. Johnson, *Nat. Photonics* **2016**, *10*, 611.
[30] D. Qian, Z. Zheng, H. Yao, W. Tress, T. R. Hopper, S. Chen, S. Li, J. Liu, S. Chen, J. Zhang, X.-K. Liu, B. Gao, L. Ouyang, Y. Jin, G. Pozina, I. A. Buyanova, W. M. Chen, O. Inganas, V. Coropceanu, J.-L. Bredas, H. Yan, J. Hou, F. Zhang, A. A. Bakulin, F. Gao, *Nat. Mater.* **2018**, *17*, 703.
[31] K. K. Paul, J.-H. Kim, Y. H. Lee, *Nat. Rev. Phys.* **2021**, *3*, 178.
[32] P. Narang, R. Sundararaman, H. A. Atwater, *Nanophotonics* **2016**, *5*, 96.
[33] N. S. Makarov, S. Guo, O. Isaienko, W. Liu, I. Robel, V. I. Klimov, *Nano Lett.* **2016**, *16*, 2349.
[34] W. Li, Y. She, A. S. Vasenko, O. V. Prezhdo, *Nanoscale* **2021**, *13*, 10239.
[35] Y. H. Jang, Y. J. Jang, S. Kim, L. N. Quan, K. Chung, D. H. Kim, *Chem. Rev.* **2016**, *116*, 14982.
[36] X. Kou, N. Xie, F. Chen, T. Wang, L. Guo, C. Wang, Q. Wang, J. Ma, Y. Sun, H. Zhang, G. Lu, *Sens. Actuators, B* **2018**, *256*, 861.
[37] Y. Yang, H. Chen, X. Zou, X.-L. Shi, W.-D. Liu, L. Feng, G. Suo, X. Hou, X. Ye, L. Zhang, C. Sun, H. Li, C. Wang, Z.-G. Chen, *ACS Appl. Mater. Interfaces* **2020**, *12*, 24845.
[38] A. Wang, S. Wu, J. Dong, R. Wang, J. Wang, J. Zhang, S. Zhong, S. Bai, *Chem. Eng. J.* **2021**, *404*.
[39] X. Li, J. Zhu, B. Wei, *Chem. Soc. Rev.* **2016**, *45*, 3145.
[40] A. O. Govorov, H. Zhang, Y. K. Gun'ko, *J. Phys. Chem. C* **2013**, *117*, 16616.
[41] A. O. Govorov, H. Zhang, H. V. Demir, Y. K. Gun'ko, *Nano Today* **2014**, *9*, 85.
[42] B. S. Karasik, S. V. Pereverzev, A. Soibel, D. F. Santavicca, D. E. Prober, D. Olaya, M. E. Gershenson, *Appl. Phys. Lett.* **2012**, *101*, 052601.
[43] J. K. Choi, V. Mitin, R. Ramaswamy, V. A. Pogrebnyak, M. P. Pakmehr, A. Muravjov, M. S. Shur, J. Gill, I. Mehdi, B. S. Karasik, A. V. Sergeev, *IEEE Sens. J.* **2013**, *13*, 80.
[44] J. Wu, M. Habibi, *Eng. Comput.* **2022**, *38*, 4127.
[45] X. F. Li, H. B. Li, L. W. Liu, Y. Q. Liu, M. H. Ju, J. Zhao, *Int. J. Rock Mech. Min. Sci.* **2020**, *127*, 104129.
[46] X. Han, H. Li, Y. Zhou, L. Wang, S. Liang, F. Javaid, *Prog. Electromagn. Res.* **2022**, *175*, 13.
[47] A. D. Rakic, A. B. Djurisic, J. M. Elazar, M. L. Majewski, *Appl. Opt.* **1998**, *37*, 5271.
[48] M. R. Querry, Optical Constants, Contractor Report CRDC-CR-85034 **1985**.
[49] A. Tittl, M. G. Harats, R. Walter, X. Yin, M. Schaeferling, N. Liu, R. Rapaport, H. Giessen, *ACS Nano* **2014**, *8*, 10885.